

Seamless maps of major elements of the Moon: Results from high-resolution geostationary satellite

Yu Lu^{1,2,3}, Yun-Zhao Wu^{1,4*}, Cui Li¹, Jin-Song Ma^{5,6}, Wen-Wen Qi⁷, Wei Tan⁷, Xiao-Man Li⁷, Zhi-Cheng Shi⁷, Hong-Yan He⁷, Shu-Wu Dai⁸, Guo Li⁸, Feng-Jing Liu⁸, Jing-Qiao Wang⁹, Xiao-Yan Wang⁹, Qi Wang¹⁰ and Ling-Jie Meng¹⁰

- ¹ Key Laboratory of Planetary Sciences, Purple Mountain Observatory, Chinese Academy of Sciences, Nanjing 210034, China; wu@pmo.ac.cn
² School of Astronomy and Space Science, University of Science and Technology of China, Hefei 230026, China
³ CAS Center for Excellence in Comparative Planetology, Hefei 230026, China
⁴ Space Science Institute, Macau University of Science and Technology, Macau, China
⁵ School of Geography and Ocean Science, Nanjing University, Nanjing 210023, China
⁶ Jiangsu Center for Collaborative Innovation in Geographical Information Resource Development and Application, Nanjing 210023, China
⁷ Beijing Institute of Space Mechanics and Electricity, Beijing 100076, China
⁸ Beijing Institute of Spacecraft System Engineering, Beijing 100076, China
⁹ China Centre for Resources Satellite Data and Application, Beijing 100094, China
¹⁰ Earth Observation System and Data Center, China National Space Administration, Beijing 100010, China

Received 2020 May 23; accepted 2020 July 29

Abstract Major elements such as Fe, Ti, Mg, Al, Ca and Si play very important roles in understanding the origin and evolution of the Moon. Previous maps of these major elements derived from orbital data are based on mosaic images or low-resolution gamma-ray data. The hue variations and gaps among orbital boundaries in the mosaic images are not conducive to geological studies. This paper aims to produce seamless and homogenous distribution maps of major elements using the single-exposure image of the whole lunar disk obtained by China's high-resolution geostationary satellite, Gaofen-4, with a spatial resolution of ~ 500 m. The elemental contents of soil samples returned by Apollo and Luna missions are regarded as ground truth, and are correlated with the reflectance of the sampling sites extracted from Gaofen-4 data. The final distribution maps of these major oxides are generated with the statistical regression model. With these products, the average contents and proportions of the major elements for maria and highlands were estimated and compared. The results showed that SiO_2 and TiO_2 have the highest and lowest fractions in mare and highland areas, respectively. Moreover, the relative concentrations of these elements could serve as indicators of geologic processes, e.g., the obviously asymmetric distributions of Al_2O_3 , CaO and SiO_2 around Tycho crater may suggest that Tycho crater was formed by an oblique impact from the southwest direction.

Key words: Moon — Data analysis — Imaging spectroscopy

1 INTRODUCTION

Information on the global chemistry of major elements such as Fe, Ti, Mg, Al, Ca and Si is fundamentally significant for understanding the composition, origin and evolution of the Moon, and thus is an important scientific objective in lunar exploration. The classic Lunar Magma Ocean theory believes that the Moon was initially molten. During the cooling of the Moon, dense magnesium

silicates olivine and pyroxene crystallized first and sank to the bottom of the magma ocean, forming the lunar mantle. The remaining magma became increasingly rich in calcium and aluminum until plagioclase began to crystallize and float to the surface of the magma ocean, forming the highlands crust (Wood et al. 1970; Warren 1985, 1990; Carlson 2019). Of the six major elements, Fe and Mg are rich in olivine and pyroxene in the mantle, while Al and Ca are abundant in plagioclase in the lunar

crust. Mapping the crustal distributions of these major elements is beneficial for understanding the geochemical composition and geological evolution of the bulk Moon.

Lunar samples provide the most direct and accurate information about the elements of the Moon. However, these samples are very limited considering the large scope of the Moon. Remote sensing technology is widely employed to explore the spatial distribution of the elements on the Moon. Among these six elements, Fe and Ti are transition elements, which exhibit absorption features and could be quantitatively estimated with optical spectroscopy. The distributions of FeO and TiO₂ contents have been derived by many researchers utilizing different data, such as Clementine ultraviolet-visible (UV/VIS) images (Lucey et al. 1995, 2000; Blewett et al. 1997; Gillis et al. 2004; Gillis-Davis et al. 2006), Hubble Space Telescope data (Robinson et al. 2007), Chang'E-1 Interference Imaging Spectrometer (IIM) data (Wu 2012; Wu et al. 2012; Xia et al. 2019), Chang'E-2 microwave sounder data (Liu et al. 2019), Kaguya Multiband Imager data (Otake et al. 2012; Lemelin et al. 2016), Chandrayaan-1 Moon Mineralogy Mapper (M³) data (Bhatt et al. 2019) and Lunar Reconnaissance Orbiter Camera Wide Angle Camera data (Sato et al. 2017). Although non-chromophore elements, such as Mg, Al, Ca and Si, do not have diagnostic absorption features, they can also affect the Moon's reflectance values, and thus could be estimated by optical spectroscopy (Fischer & Pieters 1995; Shkuratov et al. 2003, 2005; Wu 2012). Fischer & Pieters (1995) mapped the Al concentrations on the Moon by Galileo solid state imaging system based on the positive correlation between lunar surface reflectance and aluminum concentration. Bhatt et al. (2019) mapped the abundances of Fe, Ca and Mg using M³ data. Various methods, such as principal component analysis (Jaumann 1991), principal component regression (Pieters et al. 2002), partial least squares regression (Li 2006; Wu 2012), support vector machine (Zhang et al. 2009; Bhatt et al. 2019), second-order polynomial regression model (Wöhler et al. 2011), multivariate linear regression (Bhatt et al. 2019) and neural networks model (Xia et al. 2019), have been applied to estimate these major elements, and their predictions are quite successful.

Optical spectroscopy can be applied for producing high resolution maps of major elements. Shkuratov et al. (2005) generated global maps of major elements with Clementine UV/VIS images. Wu (2012) and Xia et al. (2019) produced maps of the abundances of the six major elements and Mg# (the molar or atom ratio of Mg/(Mg+Fe)) utilizing Chang'E-1 IIM data. However, these maps have mosaic borders due to calibration and photometric artifacts or gaps due to lack of data (e.g., Clementine, M³ and IIM results). The hue variations and gaps among orbital boundaries in the mosaic images

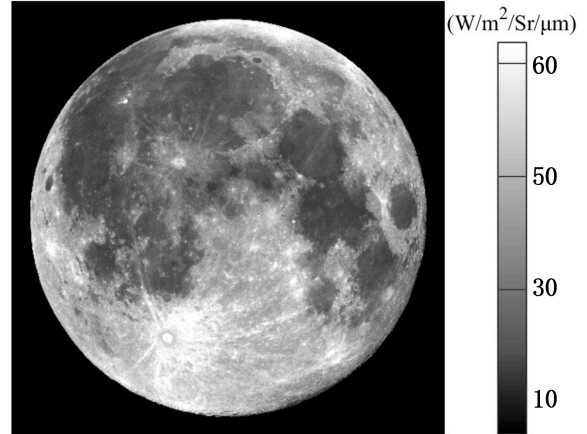


Fig. 1 The radiance of the Moon imaged by the GF-4 band 5 on 2018 July 28 (Wu et al. 2020).

are not conducive to geological studies, e.g., separation of different geologic units. This study aims to produce seamless and homogeneous maps of major elements using the single-exposure image of the whole lunar disk obtained by the high-resolution geostationary satellite Gaofen-4 (GF-4).

2 DATA AND METHOD

2.1 Data

GF-4 is the first high-resolution geostationary satellite in China. It has six spectral channels: 450 ~ 900 nm (band 1) in panchromatic, 450 ~ 520 nm (band 2) in blue, 520 ~ 600 nm (band 3) in green, 630 ~ 690 nm (band 4) in red, 760 ~ 900 nm (band 5) in near-infrared and 3.5 ~ 4.1 μm (band 6) in mid-infrared. GF-4 has a large-array Visible and Near Infrared (VNIR) detector with a field of view (FOV) of 0.8° × 0.8° and instantaneous fields of view (IFOV) of 1.363 μrad pixel⁻¹. At 04:49:00 UTC on 2018 July 28, GF-4 imaged the Moon in visible and near-infrared (bands 1-5) with spatial resolution of ~ 500 m (Wu et al. 2020) (Fig. 1). (The GF-4 images of Copernicus crater derived at four different local times are shown in Fig. A.1 as an example.) In this observation, the Moon-Sun distance is 1.015 AU, the Moon-Camera distance is 44.581 × 10⁴ km, the sub-solar point is 0.02° S, 4.77° W, the sub-camera point is 1.47° S, 1.17° W and the phase angle is 3.88°. This study used band 5 (near-infrared) data to estimate the contents of the major elements since in this band the Moon has relatively higher energy. The lunar effective wavelength for band 5 is 0.81 μm.

The reflectance data were calculated applying the equation below

$$Ref = \frac{RAD \times \pi \times d^2}{E} \times \frac{\mu_0 + \mu}{\mu_0} \quad (1)$$

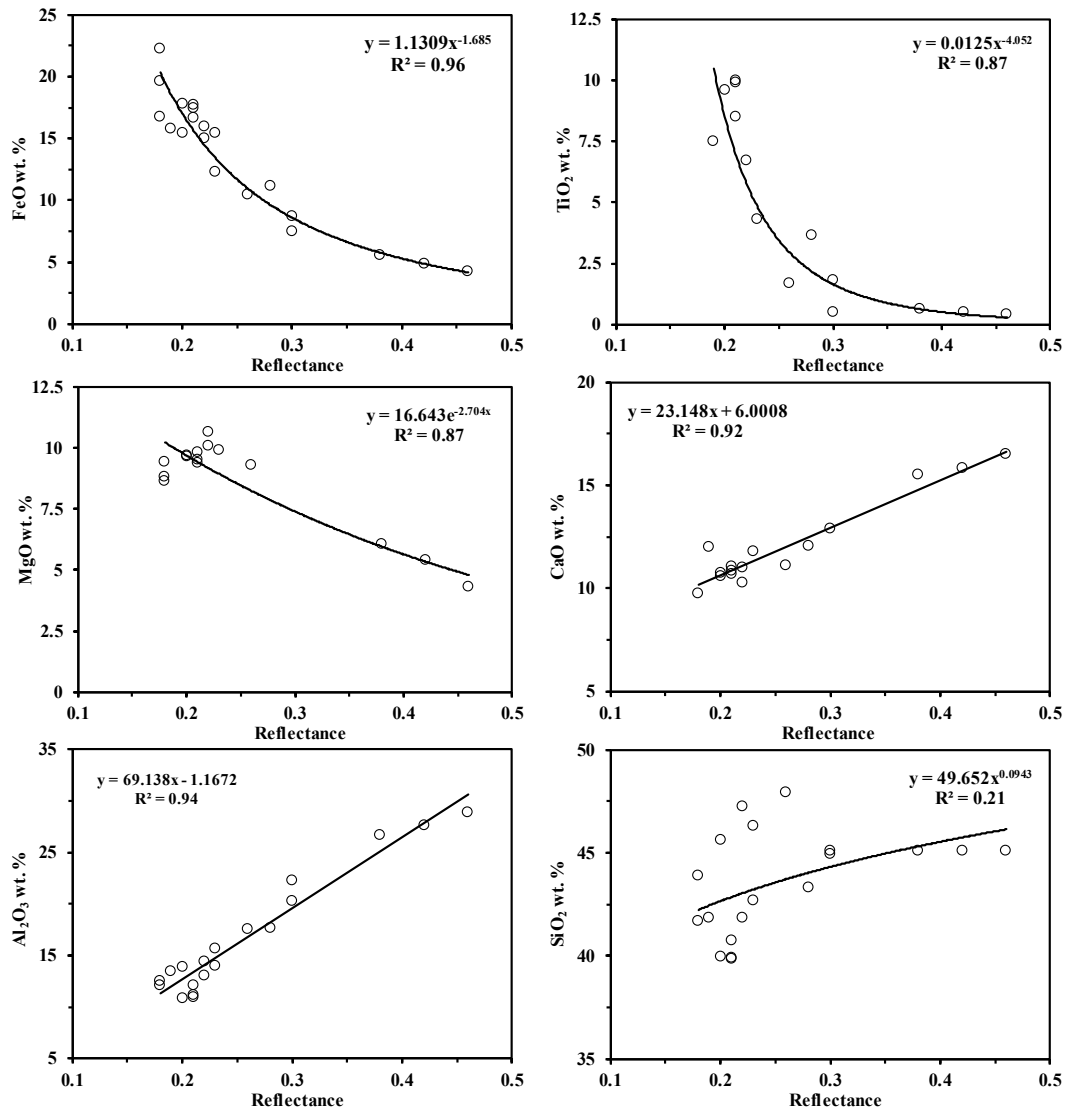


Fig. 2 The relationships between the GF-4 band 5 reflectance and the abundances of the six major elements of the samples in Table 1.

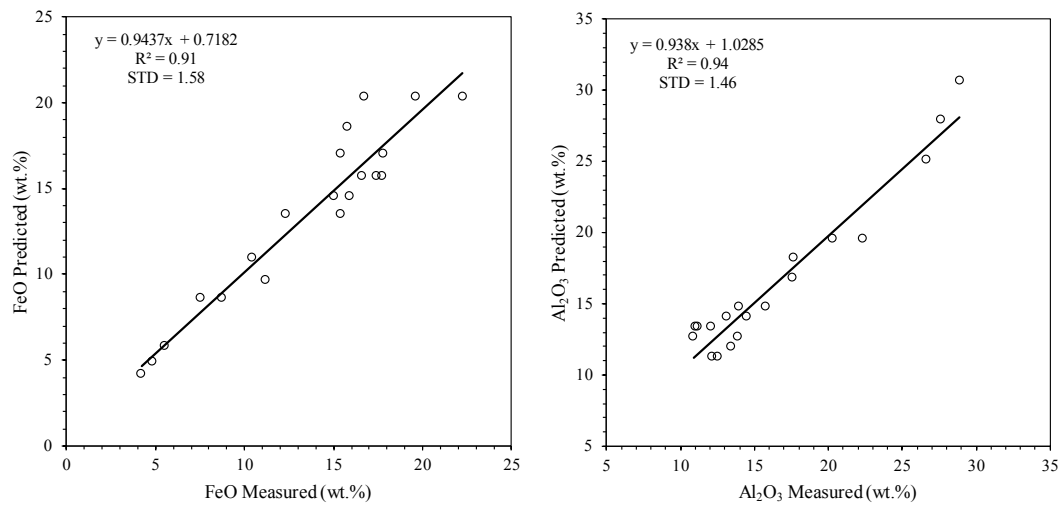


Fig. 3 Plots of predicted vs. measured abundances of FeO and Al₂O₃.

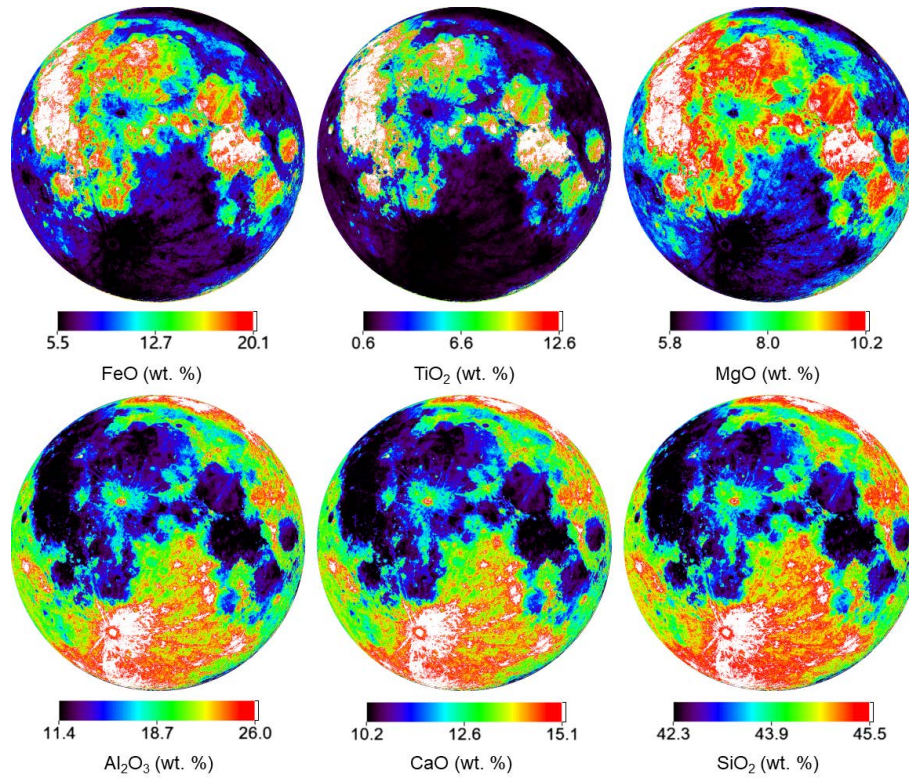


Fig. 4 Maps of the abundances of the major elements on the lunar nearside derived from GF-4 data.

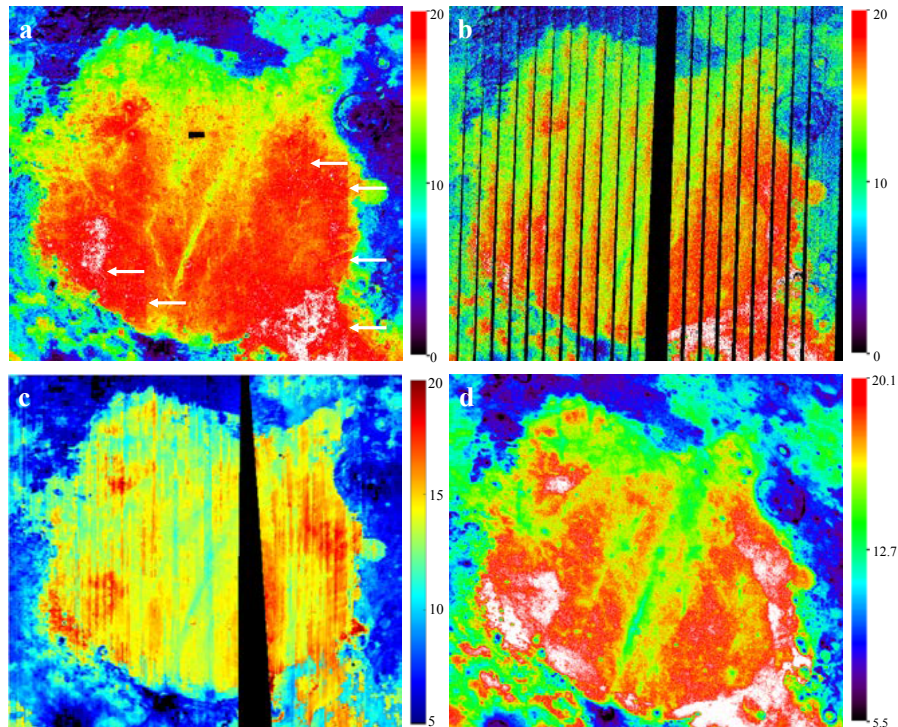


Fig. 5 Comparison of FeO abundances in different data sets in the Mare Serenitatis region. (a) FeO abundance map derived from Clementine (Lucey *et al.* 2000). (b) FeO abundance map derived from Chang'E-1 IIM (Wu 2012). (c) FeO abundance map derived from M³ (modified from Bhatt *et al.* (2019)). (d) FeO abundance map derived from GF-4. White arrows in (a) point out the hue variations around the mosaic borders, which are very prominent in (b) and (c). Black cubes indicate the gaps due to lack of data.

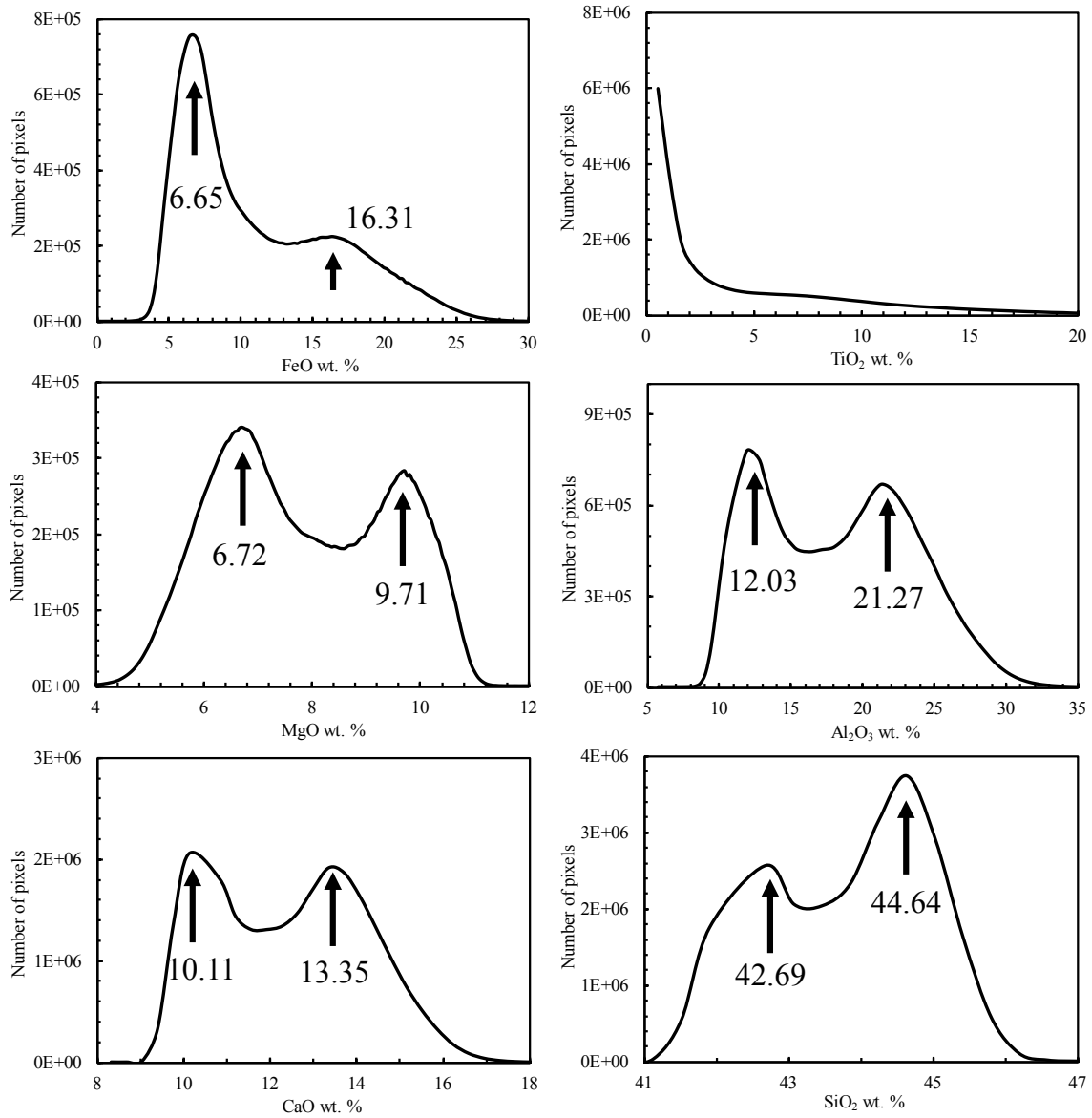


Fig. 6 Histograms of elemental abundances for the lunar nearside derived from GF-4 data.

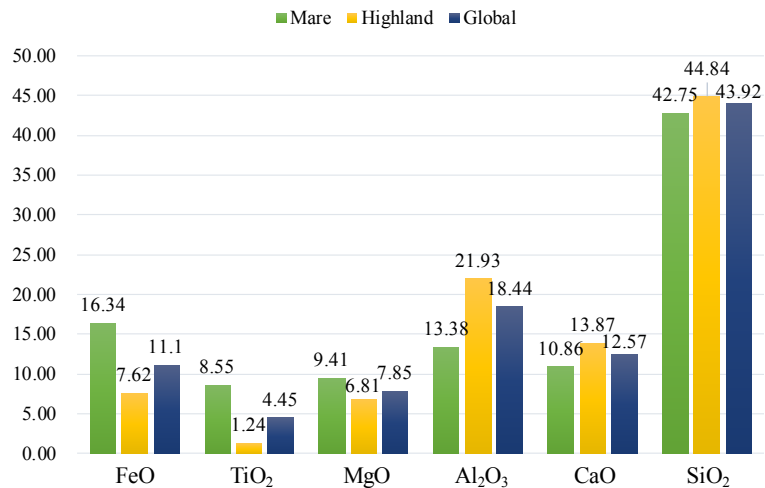
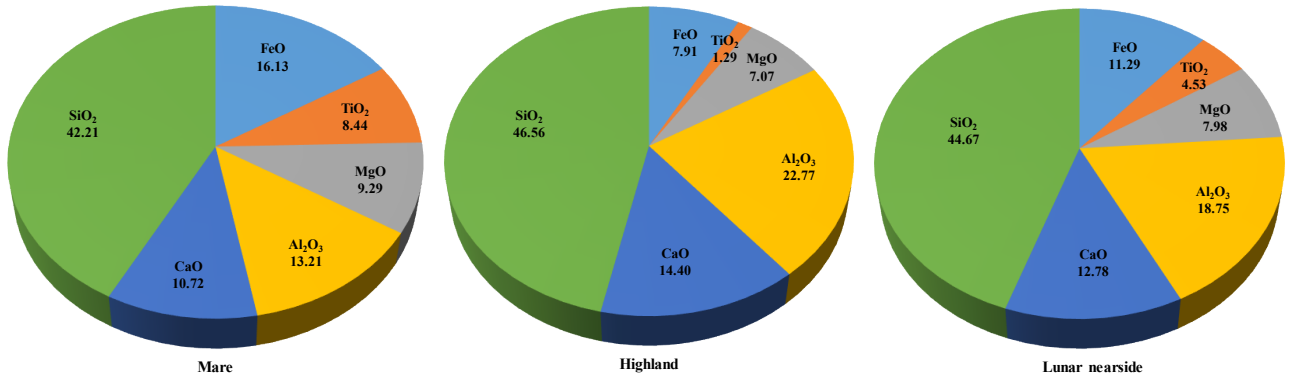


Fig. 7 Average abundances of the six major elements derived from GF-4 data.

Table 1 Major Elemental Abundances for Lunar Sample Sites Examined in This Study

Site	Lat	Lon	Ref	FeO	TiO ₂	MgO	CaO	Al ₂ O ₃	SiO ₂	Sample	References
Chang'E-3	44.13	340.49	0.18	22.24	4.31	8.61	9.72	12.11		Yutu rover	1
A11	0.73	23.49	0.19	15.8	7.5	7.81	12.01	13.45	41.86	10002, 10010, 10084	2, 3
A12	-2.99	336.69	0.2	15.4	3.1	9.66	10.58	13.86	45.62	12001, 12003, 12023, 12030, 12032, 12033, 12034, 12037, 12041, 12042, 12044, 12057, 12070	3, 4
A14 LM-Cone	-3.66	342.62	0.26	10.4	1.67	9.29	11.12	17.57	47.94	14003, 14148, 14149, 14156, 14049, 14163, 14240, 14259, 14421	3, 5
A15 LM	26.14	3.67	0.22	15	1.9	10.65	10.25	14.45		15021, 15013	6
A15S1-9	26.06	3.66	0.23	15.4	1.51	11.19	10.05	13.96		15071, 15101, 15201, 15211, 15221, 15231, 15471, 15241, 15261, 15271, 15291, 15301, 15411, 15031, 15041, 15501, 15511, 15531, 15601	6, 7
A16S1-9	-9.03	15.49	0.38	5.5	0.61	6.04	15.51	26.67	45.07	61141, 61161, 61241, 61281, 61501, 62241, 62281, 64421, 64501, 65501, 65701, 65901, 66041, 66081, 68121, 68501, 68821, 68841, 69921, 69941, 69961	8
A16S11	-8.81	15.51	0.46	4.2	0.4	4.3	16.5	28.9	45.1	61141, 61161, 61241, 61281, 61501	8
A16S13	-8.83	15.52	0.42	4.8	0.5	5.4	15.8	27.6	45.1	63321, 63341, 63501	8
A17LM	20.19	30.74	0.21	16.6	8.5	9.8	11.04	12.07	40.73	70019, 70161, 70181, 70011	9, 10
A17S1	20.16	30.75	0.2	17.8	9.6	9.62	10.75	10.87	39.93	71501, 71041, 71061, 71131, 71151	9, 11
A17S3	20.17	30.53	0.3	8.7	1.8	10.25	12.89	20.29	44.94	73221, 73241, 73261, 73281	10
A17S5	20.19	30.69	0.21	17.7	9.9	9.51	10.85	10.97	39.86	75061, 75081	9
A17S6-7	20.29	30.78	0.28	11.15	3.65	10.54	12.05	17.67	43.3	76241, 76261, 76281, 76321, 76501, 77531	9
A17S8	20.28	30.85	0.23	12.3	4.3	9.91	11.77	15.73	42.67	78501	9
A17LRV7-8	20.21	30.65	0.22	15.9	6.7	10.06	11	13.1	41.85	75111, 75121	11
A17LRV12	20.20	30.78	0.21	17.4	10	9.36	10.7	11.15	39.9	70311, 70321	11
Luna16	-0.71	56.37	0.18	16.7	3.3	8.8	12.5	15.3	41.7		3
Luna20	3.54	56.44	0.3	7.5	0.5	9.8	15.1	22.3	45.1		3
Luna24	12.75	62.04	0.18	19.6	1	9.4	12.3	12.5	43.9		3

References: 1. Wu et al. (2018); 2. Rhodes & Blanchard (1982); 3. Heiken et al. (1991); 4. Frondel et al. (1971); 5. Rose et al. (1972); 6. Korotev (1987); 7. Cuttitta et al. (1973); 8. Korotev (1981); 9. Rhodes et al. (1974); 10. Rose et al. (1974); 11. Korotev & Kremser (1992); 12. Korotev et al. (2003).

**Fig. 8** Pie charts illustrating the proportion of the abundances of the major elements in maria, highlands and the lunar nearside.

where Ref is reflectance, RAD is the radiance, $\mu_0 = \cos i$, i is the solar zenith angle, $\mu = \cos e$, e is the satellite zenith angle, and d represents the distance between the Sun and the Moon. E is the solar irradiance at 1 AU, and was

resampled according to the wavelength of GF-4 band 5

$$E = \frac{\int_{\lambda_1}^{\lambda_2} J_{\lambda} S_b(\lambda) d\lambda}{\int_{\lambda_1}^{\lambda_2} S_b(\lambda) d\lambda} \quad (2)$$

where E is the resampled solar irradiance of GF-4 band 5, J_λ is the original solar flux and $S_b(\lambda)$ is the spectral response function of band 5.

The elemental contents of soil samples returned by Apollo and Luna missions were regarded as ground truth and correlated with the reflectance of the sampling sites extracted from the GF-4 data. In addition to the sample sites described in Wu (2012), the Chang'E-3 site (Wu et al. 2018) and two Apollo 15 sites were also considered in this study (Table 1). The sampling station coordinates come from Wu (2012), and detailed elemental contents at these sample sites are from the references listed in Table 1. However, some of the Apollo 15, 16 and 17 sampling sites cannot be resolved in the GF-4 image, thus the elemental contents at some sampling sites were averaged. The reflectance value of each sample station was manually extracted from the GF-4 data considering its latitude, longitude and the published traverse maps.

2.2 Method

A statistical regression model was applied to predict the contents of all the six elements. The elemental contents from soil sample stations were plotted against the reflectance values of GF-4, and five univariate regression models, including linear, power law, exponential, logarithmic and polynomial models, were applied to fit the plots with the least squares method. Note that obvious outliers would decrease the prediction accuracy, and thus were omitted. The best model was determined according to the squared correlation coefficient (R^2). The best-fit lines provided the calibration from the GF-4 reflectance values to absolute major element contents, and were used to produce the abundance maps of these major elements. The standard deviation (STD) of the elements is defined as (Lucey et al. 2000)

$$\left\{ \left[\sum (\text{Element}_{\text{predicted}} - \text{Element}_{\text{actual}})^2 \right] / (N - 1) \right\}^{0.5} \quad (3)$$

where N is the number of stations.

3 RESULTS

3.1 Maps of the Major Elements

Figure 2 plots the relationships between the GF-4 reflectance and the abundances of the major elements in the lunar samples established in this study. The GF-4 reflectance decreases with the increasing abundances of FeO, TiO₂ and MgO, but increases along with the increase of the Al₂O₃, CaO and SiO₂ abundances. The best-fit models are power law for FeO, TiO₂ and SiO₂, exponential for MgO, and linear for CaO and Al₂O₃. Except for SiO₂, all the R^2 values are ≥ 0.87 , and even greater than 0.92 for

FeO, CaO and Al₂O₃, indicating that it fits well. Figure 3 shows the plots of predicted versus measured abundances of FeO and Al₂O₃ at the sample stations. Both the slope and the R^2 are > 0.9 , indicating the model applied in this study achieves a relatively good performance in predicting the elemental contents. The STDs for FeO and Al₂O₃ are 1.58 and 1.46 respectively, comparable with those in Lucey et al. (2000) and Wu (2012).

Figure 4 displays the maps of the elemental contents on the lunar nearside produced using the models established above. Compared with previous maps produced by Clementine (Lucey et al. 1995, 2000; Blewett et al. 1997; Gillis et al. 2004, 2006), M³ (Bhatt et al. 2019) or Chang'E-1 IIM (Wu 2012; Xia et al. 2019), it is obvious that the maps derived in this study are seamless and homogenous, without hue variations or gaps (Fig. 5). The abundances of the major elements in this study are comparable with previous results. The abundance of FeO is ~ 5.5 –20.1 wt.% in this study, it is ~ 2.1 –16.4 wt.% in Wu (2012), ~ 0 –20 wt.% in Lucey et al. (2000) and Wu et al. (2012), and ~ 2.5 –22.5 wt.% in Lemelin et al. (2016). The abundance of TiO₂ in this study is ~ 0.6 –12.6 wt.%, and it is ~ 0 –8 wt.% in Wu (2012) and ~ 2 –10 wt.% in Sato et al. (2017). Note that the maps in this study only covered the lunar nearside, there may exist some differences, e.g., the lower limit of the abundance of FeO is a little higher than other results.

The spectrally unique and unsampled Eratosthenian basalts distributed in Mare Imbrium (including the Chang'E-3 landing zone), Oceanus Procellarum and Mare Tranquillitatis are prominent in the maps of elemental contents (Fig. 4). These basalts have the highest FeO, TiO₂ and MgO abundances (white color in Fig. 4), different from other mare basalts. Mare basalts in Mare Tranquillitatis are the same. The high resolution maps of these major elements produced in this study clearly exhibit these differences, and thus are beneficial for geologic studies, e.g., division of different geologic units.

Maria, such as Mare Imbrium, Oceanus Procellarum, Mare Serenitatis and Mare Tranquillitatis, are generally abundant in FeO, TiO₂ and MgO. However, Mare Frigoris is an exception. Compared with other maria, the average TiO₂ content in Mare Frigoris (~ 2.91 wt.%) is much lower, and the average Al₂O₃ content (~ 17.24 wt.%) is higher, indicating that most of the basalts in Mare Frigoris are high-Al basalts (Kramer et al. 2015).

The abundance maps of the major elements, especially Al₂O₃, CaO and SiO₂, clearly display the ejecta distribution of Tycho crater (Fig. 4). The bottom and eastern parts of Tycho crater are rich in Al₂O₃, CaO and SiO₂, while the contents of these elements on the crater wall and the western part of the crater are relatively lower. The asymmetric distributions of these major elements around Tycho crater may suggest that Tycho crater was

formed by an oblique impact from the southwest direction, consistent with studies on the distributions of impact melt and secondary craters of Tycho (Hirata et al. 2004; Krüger et al. 2016). The abundances of Al_2O_3 , CaO and SiO_2 on the relatively fresh ejecta of Tycho crater are higher than the abundances on the surrounding highland areas, which may be due to space weathering effects.

3.2 Statistical Analysis

Figure 6 shows the abundance distributions of all the six major elements. Except for TiO_2 , which features a unimodal continuum distribution, all other elements exhibit bimodal distributions, corresponding to the maria and highlands respectively, consistent with previous studies (Lucey et al. 1998; Giguere et al. 2000; Gillis et al. 2004; Wu 2012; Wu et al. 2012). The lower modal Fe abundance of ~ 6.65 FeO wt.% and the higher modal Fe abundance of ~ 16.31 FeO wt.%, which correspond to the highland areas and mare areas respectively, are a little higher than the abundance of ~ 5.57 wt.% given by Wu (2012), or ~ 5.7 wt.% by Gillis et al. (2004), consistent with the fact that the maps in this study only covered the lunar nearside, and the abundances of FeO on the lunar farside (mostly highland areas) are much lower than on the nearside. Moreover, the average abundances of these major elements in maria, highlands and the whole lunar nearside were estimated and compared (Fig. 7). The abundances of FeO, TiO_2 and MgO in the maria are higher than those in the highlands, while the abundances of Al_2O_3 , CaO and SiO_2 are opposite. Figure 8 depicts the proportion of the abundances of the major elements in maria, highlands and the whole lunar nearside. As can be seen, both in maria and highlands, SiO_2 has the highest proportion ($> 40\%$) among these major elements, while TiO_2 has the lowest proportion ($< 10\%$), e.g., TiO_2 only makes up 1.29% of elements in the highlands.

4 CONCLUSIONS

China's high-resolution geostationary satellite, GF-4, imaged the whole lunar disk with spatial resolution of ~ 500 m in a single exposure. Using these data, this study produced the seamless and homogeneous distribution maps of the abundances of the major elements (Fe, Ti, Mg, Al, Ca, Si) on the lunar nearside. Compared with previous maps, the maps derived in this study show no hue variations or gaps, and thus are more beneficial for geologic studies, e.g., division of different geologic units. With these products the average contents and proportions of the major elements for mare and highland areas were estimated and compared. The results affirmed that both in maria and highlands, SiO_2 has the highest proportion among these major oxides, while TiO_2 has the lowest. The asymmetric distributions of Al_2O_3 , CaO and SiO_2 around

Tycho crater may suggest that Tycho crater was formed by an oblique impact from the southwest direction. Some related geological researches will be carried out in the future based on the products produced in this study.

Acknowledgements We would like to thank the China National Space Administration (CNSA) for organizing the observations. This research was supported by the National Key R&D Program of China (2018YFB0504700), the National Natural Science Foundation of China (Grant No. 42050202), the pre-research project on Civil Aerospace Technologies by CNSA (D020203), the Macau Science and Technology Development Fund (0090/2020/A, 0042/2018/A2) and Minor Planet Foundation of Purple Mountain Observatory.

Appendix A:

References

- Bhatt, M., Wöhler, C., Grumpe, A., et al. 2019, *A&A*, 627, A155
- Blewett, D. T., Lucey, P. G., Hawke, B. R., et al. 1997, *J. Geophys. Res.*, 102, 16319
- Carlson, R. W. 2019, *Science*, 365, 240
- Cuttitta, F., Rose, H. J., J., Annell, C. S., et al. 1973, in *Lunar and Planetary Science Conference Proceedings*, 4, 1081
- Fischer, E. M., & Pieters, C. M. 1995, *J. Geophys. Res.*, 100, 23279
- Frondel, C., Klein, C., J., & Ito, J. 1971, in *Lunar and Planetary Science Conference Proceedings*, 2, 719
- Giguere, T. A., Taylor, G. J., Hawke, B. R., et al. 2000, *Meteoritics and Planetary Science*, 35, 193
- Gillis-Davis, J. J., Lucey, P. G., & Hawke, B. R. 2006, *Geochim. Cosmochim. Acta*, 70, 6079
- Gillis, J. J., Jolliff, B. L., & Korotev, R. L. 2004, *Geochim. Cosmochim. Acta*, 68, 3791
- Heiken, G. H., Vaniman, D. T., & French, B. M. 1991, *Lunar Sourcebook, A User's Guide to the Moon* (Cambridge: Cambridge Univ. Press)
- Hirata, N., Nakamura, A. M., & Saiki, K. 2004, in *Lunar and Planetary Science Conference*, eds. S. Mackwell, & E. Stansbery, 1587
- Jaumann, R. 1991, *J. Geophys. Res.*, 96, 22793
- Korotev, R. L. 1981, *Lunar and Planetary Science Conference*, 565
- Korotev, R. L. 1987, *J. Geophys. Res.*, 92, E411
- Korotev, R. L., & Kremser, D. T. 1992, in *Lunar and Planetary Science Conference*, 22, 275
- Korotev, R. L., Jolliff, B. L., Zeigler, R. A., et al. 2003, *Geochim. Cosmochim. Acta*, 67, 4895
- Kramer, G. Y., Jaiswal, B., Hawke, B. R., et al. 2015, *Journal of Geophysical Research (Planets)*, 120, 1646
- Krüger, T., van der Bogert, C. H., & Hiesinger, H. 2016, *Icarus*, 273, 164

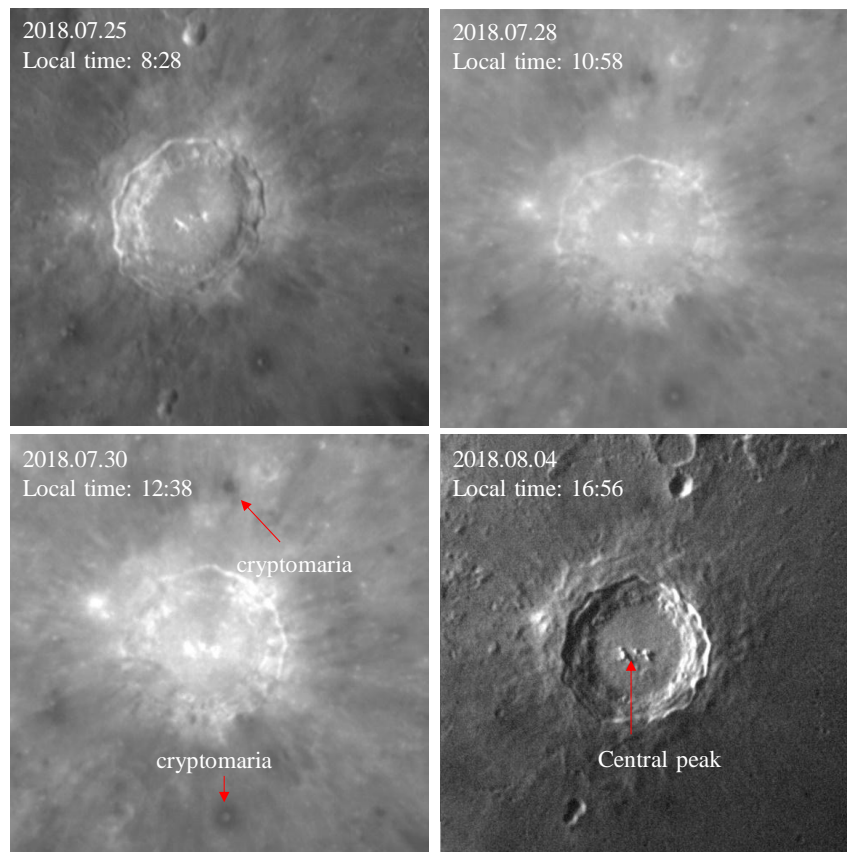


Fig. A.1 Copernicus crater imaged by GF-4 satellite at four different local times.

- Lemelin, M., Lucey, P. G., Gaddis, L. R., et al. 2016, in Lunar and Planetary Science Conference, 2994
- Li, L. 2006, *Journal of Geophysical Research (Planets)*, 111, E04002
- Liu, C., Sun, H.-Y., Meng, Z.-G., et al. 2019, *RAA (Research in Astronomy and Astrophysics)*, 19, 066
- Lucey, P. G., Taylor, G. J., & Malaret, E. 1995, *Science*, 268, 1150
- Lucey, P. G., Blewett, D. T., & Hawke, B. R. 1998, *J. Geophys. Res.*, 103, 3679
- Lucey, P. G., Blewett, D. T., & Jolliff, B. L. 2000, *J. Geophys. Res.*, 105, 20297
- Otake, H., Ohtake, M., & Hirata, N. 2012, in Lunar and Planetary Science Conference 1905
- Pieters, C. M., Stankevich, D. G., Shkuratov, Y. G., & Taylor, L. A. 2002, *Icarus*, 155, 285
- Rhodes, J. M., Rodgers, K. V., Shih, C. Y., et al. 1974, in Lunar and Planetary Science Conference, 2, 1097
- Rhodes, J. M., & Blanchard, D. P. 1982, in Lunar and Planetary Science Conference, 12, 607
- Robinson, M. S., Hapke, B. W., Garvin, J. B., et al. 2007, *Geophys. Res. Lett.*, 34, L13203
- Rose, H. J., J., Cuttitta, F., Annell, C. S., et al. 1972, in Lunar and Planetary Science Conference, 3, 1215
- Rose, H. J., J., Cuttitta, F., Berman, S., et al. 1974, in Lunar and Planetary Science Conference, 2, 1119
- Sato, H., Robinson, M. S., Lawrence, S. J., et al. 2017, *Icarus*, 296, 216
- Shkuratov, Y. G., Pieters, C. M., Omelchenko, V. V., et al. 2003, in Lunar and Planetary Science Conference, eds. S. Mackwell, & E. Stansbery, 1258
- Shkuratov, Y. G., Kaydash, V. G., Stankevich, D. G., et al. 2005, *Planet. Space Sci.*, 53, 1287
- Warren, P. H. 1985, *Annual Review of Earth and Planetary Sciences*, 13, 201
- Warren, P. H. 1990, *American Mineralogist*, 75, 46
- Wöhler, C., Berezhnoy, A., & Evans, R. 2011, *Planet. Space Sci.*, 59, 92
- Wood, J. A., Dickey, J. S., J., Marvin, U. B., & Powell, B. N. 1970, *Geochimica et Cosmochimica Acta Supplement*, 1, 965
- Wu, Y. 2012, *Geochim. Cosmochim. Acta*, 93, 214
- Wu, Y., Wang, Z., Cai, W., & Lu, Y. 2018, *AJ*, 155, 213
- Wu, Y., Xue, B., Zhao, B., et al. 2012, *Journal of Geophysical Research (Planets)*, 117, E02001
- Wu, Y., Jin, Q., Li, C., et al. 2020, *Geophys. Res. Lett.*, <https://doi.org/10.1029/2020GL088393>
- Xia, W., Wang, X., Zhao, S., et al. 2019, *Icarus*, 321, 200
- Zhang, X.-Y., Li, C.-L., & Lü, C. 2009, *Chinese Journal of Geochemistry*, 28, 204